

Article

Tailored Nanoscale Architectures for White Light Photoelectrochemistry: Zinc Oxide Nanorod-Based Copper Oxide Heterostructures

Yu-Chih Fu, Yu-Che Chen, Chieh-Ming Wu and Vincent K. S. Hsiao * 

Department of Applied Materials and Optoelectronic Engineering, National Chi Nan University, Nantou 54561, Taiwan; s106328030@mail1.ncnu.edu.tw (Y.-C.F.); s110328017@mail1.ncnu.edu.tw (Y.-C.C.); s110328013@ncnu.edu.tw (C.-M.W.)

* Correspondence: kshsiao@ncnu.edu.tw

Abstract: This study investigates the morphological evolution, optical properties, and photoelectrochemical (PEC) performance of copper-oxide-coated ZnO nanorods under different annealing conditions. Distinct effects of annealing temperature and atmosphere on Cu₂O and CuO growth on ZnO nanorods were observed. SEM images revealed the transformation of Cu₂O from silk-like to mushroom-like structures, while CuO formed interconnecting nanomaterials. XRD and XPS analyses showed peak shifts and binding energy changes, highlighting structural and electronic modifications induced by annealing. Moreover, PEC measurements demonstrated the superior photoresponse of CuO-coated ZnO nanorods, especially under negative bias, attributed to favorable band structure, charge carrier separation, and annealing stability compared to Cu₂O-coated ones. A noteworthy discovery is that ZnO nanorods coated with CuO nanostructures, prepared under air conditions at 400 °C annealing temperature, exhibit exceptional photocurrents. Applying a 0.4 V voltage increases the photocurrent by approximately 10 mA/cm². The findings provide valuable insights into tailoring metal oxide semiconductor nanostructures for potential applications in diverse areas, including photoelectrochemistry. This study offers practical guidance on modulating nanostructure growth through annealing to enhance performance. The results hold significance for PEC water splitting and have far-reaching impacts on photocatalysis, environmental remediation, and solar cells.

Keywords: annealing conditions; copper oxide; zinc oxide nanorods; optical properties; photoelectrochemical performance; visible light absorption; charge separation; photocatalysis



Citation: Fu, Y.-C.; Chen, Y.-C.; Wu, C.-M.; Hsiao, V.K.S. Tailored Nanoscale Architectures for White Light Photoelectrochemistry: Zinc Oxide Nanorod-Based Copper Oxide Heterostructures. *Coatings* **2023**, *13*, 2051. <https://doi.org/10.3390/coatings13122051>

Academic Editors: Lahoucine Bahsis and Hafid Anane

Received: 9 November 2023

Revised: 1 December 2023

Accepted: 5 December 2023

Published: 6 December 2023



Copyright: © 2023 by the authors. Licensee MDPI, Basel, Switzerland. This article is an open access article distributed under the terms and conditions of the Creative Commons Attribution (CC BY) license (<https://creativecommons.org/licenses/by/4.0/>).

1. Introduction

The limitations of finite energy resources and the escalating environmental challenges have spurred the relentless pursuit of alternative and renewable energy sources [1]. As global energy demands continue to rise, the efficient conversion of solar energy into clean chemical fuel, particularly in the field of photoelectrochemical (PEC) cells [2–6], has emerged as a promising prospect. The ongoing advancements in PEC research allow us to apply this principle extensively in applications related to solar energy conversion and storage. However, the efficiency of PEC water splitting primarily hinges on the characteristics of the semiconductor material used as the photoelectrode or working electrode [7–9]. Despite exhibiting impressive energy conversion efficiency [10], compound semiconductors such as GaAs are susceptible to corrosion in aqueous environments. In contrast, oxide-based semiconductor photoelectrodes, while demonstrating lower energy conversion efficiency, offer superior corrosion resistance and are therefore considered ideal choices from a commercial standpoint, given their longevity [11–13]. Among oxide semiconductors, titanium dioxide (TiO₂) is a commonly used photoelectrode material [14–16]. However, its wide bandgap (3.27 eV) restricts light absorption to only the ultraviolet range of the solar spectrum, far from the high-energy regions. On the other hand, zinc oxide (ZnO) also

possesses a relatively wide bandgap (3.37 eV), but its electron mobility is 10 to 100 times that of TiO_2 [17]. This significant improvement in electron transport efficiency makes ZnO a preferred semiconductor used in photovoltaic devices [18–20].

In the pursuit of advanced materials for diverse applications, the synthesis of ZnO nanorods (NRs) has garnered considerable attention. The study by Liang et al. presents a straightforward physical vapor deposition method for the catalyst-free growth of well-aligned ZnO NRs on silicon substrates [21]. By heating ZnO powder to 900 °C in a horizontal tube furnace, the nanorods were obtained through a vapor–solid mechanism. The method exhibited good crystallinity and optical properties, offering potential for scalable fabrication in electronic and optical devices. Prete et al. conducted a detailed study on ZnO NR growth using gold catalyst nanoparticles and the carbo-thermal evaporation technique [22]. The findings provide crucial insights into growth kinetics and mechanisms, guiding precise engineering of ZnO NRs for optimal size and morphology control on Si substrates, which is essential for subsequent device integration. Yatsui et al. demonstrated a low-temperature (270 °C) vapor-phase technique for epitaxial growth of vertically aligned single-crystalline ZnO NRs on Si substrates [23]. Utilizing photo-assisted metal–organic vapor-phase epitaxy (MOVPE) with 325 nm laser illumination, they achieved anisotropic nanorod growth along the [001] direction. This approach, performed at low temperatures, shows promise for integrated ZnO nanostructures on Si, offering significant implications for nanophotonic and electronic devices.

The major limitation of ZnO used in PEC applications lies in its larger bandgap, resulting in limited light absorption, primarily in the ultraviolet range, away from the high-energy regions of the solar spectrum. To overcome this limitation, researchers have begun to incorporate metal dopants into ZnO to enhance their performance [24,25]. Copper (Cu) is one of the extensively studied dopants due to its reputation as an active and cost-effective co-catalyst [26]. Copper shares a similar electronic band structure with ZnO, significantly improving its photoactivity [27]. However, the effects of Cu doping on ZnO stability and efficiency in PEC water splitting remain open questions [28–30]. The investigation of PEC behavior of CuO-ZnO core/shell heterostructure nanowire arrays was first reported by Zhao et al. [31]. The CuO nanowires (NWs) were synthesized through the oxidation of copper foil in an ambient air environment. The process involved the thermal oxidation of copper foil at 500 °C for a duration of 4 h. Subsequently, after cooling to room temperature, several droplets of a saturated ethanol solution of zinc acetate were carefully applied to the prepared CuO NW arrays, followed by air drying. To achieve the desired structure, the zinc acetate-coated CuO NWs were subjected to a final thermal treatment at 350 °C for 20 min in an air environment. A scalable method for producing three-dimensional (3D) branched nanowires (b-NWs) consisting of ZnO/CuO heterojunctions was reported by Kargar et al. [32]. These b-NWs serve as photocathodes for PEC solar hydrogen production in neutral environments. The growth of ZnO/CuO b-NWs was achieved using cost-effective thermal oxidation and hydrothermal growth techniques. These b-NWs exhibit a defect-free single-crystalline structure with smooth surfaces. The study establishes a relationship between electrode currents and nanowire sizes and densities, with longer and denser CuO NW cores demonstrating higher photocathodic currents due to an enlarged reaction surface area. ZnO/CuO b-NW photoelectrodes show a broad photoresponse spectrum, spanning from ultraviolet to near-infrared. Importantly, they outperform CuO nanowires coated with ZnO in a core/shell configuration thanks to increased surface area and enhanced gas evolution. Remarkably, when grown on copper mesh substrates, ZnO/CuO b-NWs exhibit a significant enhancement in photocathodic current.

Bai et al. [33] developed a novel 3D ZnO/Cu₂O NW photocathode material with remarkably efficient photoelectrocatalytic performance. The fabrication process was achieved on a copper substrate using straightforward and cost-effective wet chemical oxidation and hydrothermal growth techniques. In comparison to pure Cu₂O NWs, the 3D ZnO/Cu₂O NWs exhibited a significantly higher photocurrent, reaching up to 4.55 mA cm². Additionally, these NWs demonstrated exceptional stability under AM 1.5G illumination at

an intensity of 100 mW/cm^2 . The outstanding performance of this unique nanostructure can be attributed to its substantial effective surface area, which facilitates efficient PEC water splitting and the degradation of organic pollutants. Moreover, the structure promotes effective electron transportation, further enhancing its potential for a wide range of applications in PEC and environmental remediation. A straightforward approach to creating a highly stable CuO/ZnO nanorod–nanobranched photocathode for the efficient generation of hydrogen through photoelectrochemical processes was reported by Shaislamov et al. [34]. The primary CuO NRs, acting as the “trunk” of the structure, were synthesized by directly thermally oxidizing Cu NRs grown using a template-assisted electrodeposition method. Subsequently, secondary ZnO nanobranched structures were uniformly grown across the entire surface of the CuO NRs using a hydrothermal method. The resulting CuO/ZnO nanorod–nanobranched photoelectrode displayed remarkable stability, retaining 90% of its performance during an extended period of testing.

The synthesis of a CuO–ZnO nanostructure through hydrothermal methods with varying Cu dopant mole ratios has been reported by Albadarin et al. [35]. These studies investigated the impact of factors such as crystallite size, surface morphology, and changes in optical band gap on the nanostructure’s PEC performance. A comparative analysis was also conducted against a reference ZnO-based photocathode. Their studies revealed a transition in the morphology of ZnO NRs, transforming into nanosheets and vertically aligned CuO–ZnO nanogrowth upon Cu incorporation. This transformation was attributed to compositional changes resulting from the excessive introduction of Cu metal into the ZnO lattice. Additionally, Cu insertion induced a bathochromic shift in the optical band gap of the sample. Evaluation of PEC activity under a 100 mW/cm^2 Xenon light source in a $0.5 \text{ M Na}_2\text{SO}_4$ electrolyte solution demonstrated that the Zn-to-Cu ratio significantly affected the photocurrent density. This enhanced performance is attributed to the larger surface area and narrower optical energy band gap in the vertically aligned CuO–ZnO nanogrowth, facilitating efficient charge transport in the PEC cells.

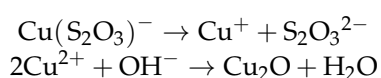
Our research focuses on the construction of copper oxide (CuO/Cu₂O) nanostructures on ZnO NRs for use in PEC applications. The key challenge in this research area lies in precisely controlling the growth of the copper oxide nanostructures to achieve higher photocurrents and improved stability. Traditional methods for fabricating PEC electrodes often involve complex processes and high material costs, limiting their feasibility for large-scale applications. However, the fabrication method employed in our research, based on the growth of ZnO nanorods and chemical bath deposition (CBD), simplifies the preparation process and significantly reduces the equipment and material costs. This unique fabrication approach opens up a new avenue for the efficient, cost-effective, and sustainable production of PEC electrodes. We have observed distinct variations in nanostructure morphology as a function of annealing temperature, specifically between samples annealed in nitrogen and air atmospheres. These observations offer valuable insights into the growth process and the role of ambient conditions in nanostructure formation. Cyclic voltammetry (CV) measurements were conducted to assess the impact of visible light irradiation on the electrochemical response of the materials. ZnO nanorods exhibited minimal changes in CV curves before and after light exposure, suggesting limited photoresponse. In contrast, Cu₂O/ZnO heterostructures with 5 and 10 CBD cycles displayed significantly increased currents and anodic peak intensities upon light exposure, indicating improved photoconversion efficiency. However, the CV of the Cu₂O/ZnO heterostructure with 15 CBD cycles showed a distinct enhancement in the cathodic peak after light irradiation. Additionally, this study investigates the effect of annealing temperatures on the nanostructure evolution and resulting photoelectrochemical (PEC) performance of Cu₂O/ZnO or CuO/ZnO heterostructures. Ultimately, we made a significant discovery: ZnO nanorods coated with CuO nanostructures prepared under an air condition at a $400 \text{ }^\circ\text{C}$ annealing temperature exhibited outstanding photocurrents. Applying a voltage of 0.4 V increased the photocurrent by approximately 10 mA/cm^2 . Annealing at different temperatures under N₂ or air conditions led to distinct nanostructure morphologies. These structural variations had a profound impact on the PEC

performance, with the high-temperature-annealed ZnO/CuO heterostructures exhibiting superior PEC properties. The significance of this discovery can be attributed to two main factors. First, the CuO layer enhances visible light absorption, enabling the material to fully harness solar energy. Second, the introduction of CuO nanostructures enhances electron transport efficiency, effectively reducing electron–hole recombination rates. Therefore, by precisely controlling the growth of nanostructures, we achieved higher photocurrents and improved stability, a facet that had not been thoroughly explored in previous research. The importance of this structural direction lies in its practical solutions for enhancing performance in the field of PEC. This not only holds great significance for PEC water splitting but also bears wide-ranging potential impacts in other PEC applications, such as photocatalysis, environmental remediation, and solar cells.

2. Materials and Methods

To prepare the indium tin oxide (ITO)-coated glass slides for deposition, we initially immersed them in commercial hydrochloric acid (37%) for 1 h. Subsequently, the slides underwent a thorough cleaning process involving acetone, ethanol, and distilled water, followed by drying in an incubator at 100 °C. We initiated the preparation of ZnO seed layers utilizing the sol-gel method [36]. Specifically, the precursor for depositing these seed layers consisted of a mixture of 15 mL of sol solution containing 0.75 M zinc acetate dihydrate ($\text{Zn}(\text{CH}_3\text{COO})_2 \cdot 2\text{H}_2\text{O}$) combined with a solvent containing equal quantities of monoethanolamine ($\text{HOCH}_2\text{CH}_2\text{NH}_2$) and 2-methoxyethanol ($\text{CH}_3\text{OCH}_2\text{CH}_2\text{OH}$). This solution was left to stabilize at room temperature for 24 h. The dip-coating process for applying the seed layer was conducted at a rate of 3 cm/min after immersing the glass slide in the sol solution for 10 min. This procedure was repeated three times. Subsequent to the dip-coating process, the substrate underwent drying and annealing on a hot plate at a temperature of 200 °C for 30 min, leading to the gelation of the sol solution on the substrate surface and subsequent seed layer formation. The growth of ZnO nanorods (NRs) was accomplished by immersing the sample in a chemical bath containing a solution of zinc nitrate hexahydrate ($\text{Zn}(\text{NO}_3)_2 \cdot 6\text{H}_2\text{O}$) and methenamine ($\text{C}_6\text{H}_{12}\text{N}_4$) at the same 0.1 M concentration, maintained at 85 °C for a duration of 2 h.

To further create heterostructure, we aimed to deposit cuprous oxide (Cu_2O) on the ZnO NRs using the chemical bath deposition (CBD) technique [37]. The CBD method allows us to achieve varying effects by adjusting the number of deposition cycles. Notably, we employed a dip coater apparatus, a departure from conventional manual operations, to ensure precise control over the deposition process. For this purpose, we employed analytical-grade copper sulfate ($\text{CuSO}_4 \cdot 5\text{H}_2\text{O}$), sodium thiosulfate ($\text{Na}_2\text{S}_2\text{O}_3 \cdot 5\text{H}_2\text{O}$), and sodium hydroxide (NaOH) in an aqueous medium. Distilled water served as our solvent. The copper–thiosulfate complex was prepared by mixing 5 mL of 1 M copper sulfate solution with 20 mL of 1 M sodium thiosulfate solution. The resulting solution was stirred for 20 min in a cold bath (approximately 0 °C) until it became colorless, serving as a source of cations. Concurrently, a 1 M NaOH solution, maintained at 75 °C, was employed as a source of anions. Each deposition cycle involved immersing the ZnO NRs/ITO glass slides first in the anion solution and then in the cation solution using controlled dip coater. The CBD procedure was conducted under carefully controlled conditions to ensure consistency across samples. The parameters governing the CBD process were kept constant, and the synthesis conditions were meticulously replicated for each sample. A controlled immersion rate of approximately 20 mm/min was maintained during the CBD process. A standardized deposition time of 10 s was maintained in anion solution, and 30 s in cation solution for all synthesis runs, ensuring consistency in the coating thickness across samples. As a result, Cu_2O thin films were formed on the substrate through the subsequent chemical reactions.



Subsequently, the slides were dipped in distilled water for 10 s to rinse away any unreacted anions and cations. After obtaining the Cu₂O/ZnO NRs nanostructure through the CBD process, we proceeded with an additional crucial step to enhance their properties, which involved annealing the materials under different atmospheres, specifically using nitrogen (N₂) gas and air. The annealing process was carried out in a controlled environment, where the copper oxide/ZnO nanomaterial samples were subjected to varying temperatures. The schematic of fabrication process of copper oxide/ZnO NRs heterostructure is shown in Figure 1a. For scanning electron microscopy (SEM) observations, a JEOL JSM-7401F field emission SEM was utilized. The instrument operated at an acceleration voltage of 15 kV, providing detailed surface morphology information. The working distance during observations was set at 3.6 mm, ensuring optimal imaging conditions. Images were acquired at various magnifications to capture both micro- and nanoscale features. Absorption spectra measurements were conducted using fiber-based UV-Vis spectrophotometer (Ocean Optics HR400HCG). This instrument is equipped with a tungsten halogen white light source. Before the absorption spectra measurements, a baseline scan was performed using a blank ITO-coated glass, which typically consisted of the substrate material without the thin film. This baseline correction accounts for any absorption or scattering effects from the substrate. X-ray diffraction (XRD) analyses were performed using a high-resolution X-ray diffractometer (PANalytical X'Pert PRO MRD). The X-ray source employed Cu K α , $\lambda = 0.15418$ nm, and diffraction patterns were recorded over a $2\theta = 20$ to 70 degree range. The instrument's parameters, including scan speed and step size, were optimized for accurate phase identification and crystallographic information. The resulting XRD patterns were analyzed to determine the structural characteristics of the synthesized materials. X-ray photoelectron spectrometer (XPS) measurements were conducted using a PHI VersaProbe 4 instrument. The X-ray source emitted Al K α X-rays of energy resolution ≤ 0.5 eV at Ag3d_{5/2} peak.

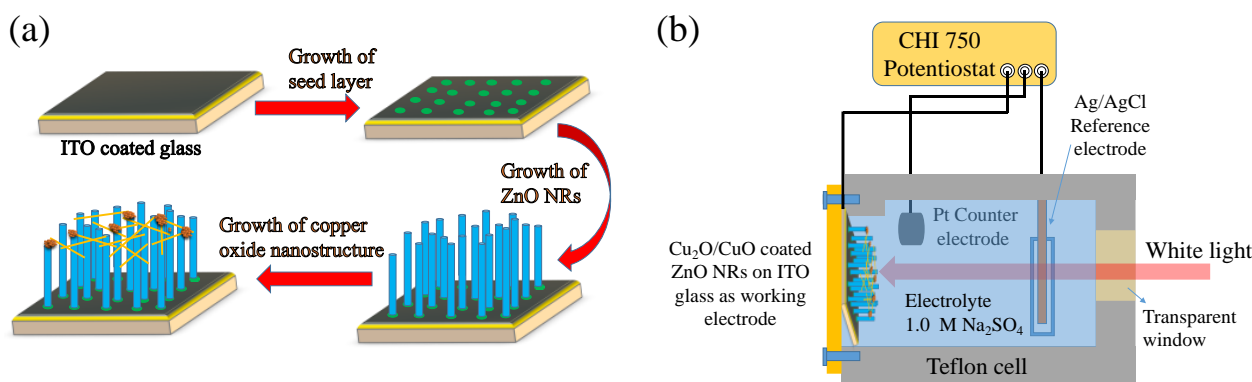


Figure 1. Schematic of (a) fabricating copper oxide/ZnO NRs heterostructure and (b) visible light photoelectrochemical measurement setup.

The experimental setup for photoelectrochemical (PEC) measurements is illustrated in Figure 1b. In this study, PEC measurements were conducted using CHI 750 potentiostat on copper oxide/ZnO nanomaterials. The electrolyte used for the PEC experiments was a 1.0 M sodium sulfate (Na₂SO₄) solution. The copper oxide/ZnO nanomaterials were assessed using a three-electrode electrochemical measurement system provided by CH Instruments. During the PEC measurements, the sample surface was illuminated with 150 W Xenon arc lamp, and an AM 1.5 filter was applied to produce 100 mW/cm² light source. The potential applied to the system was scanned from 1.0 to −1.0 V or 0.5 to −0.5 V at a scan rate of 100 mV/sec. The working electrode was connected to a reference electrode (Ag/AgCl) and a counter electrode (Pt), and a bias voltage was subsequently applied to initiate the measurement process.

3. Results

3.1. Influence of Annealing Conditions on the SEM Morphology and Optical Properties of Copper-Oxide-Coated ZnO Nanorods

Figure 2 shows the surface and cross-sectional SEM images of as-growth ZnO NRs before the CBD of copper oxide. The diameter of hexagonal-shape and length of ZnO NRs are 100 nm and 2 μm , respectively.

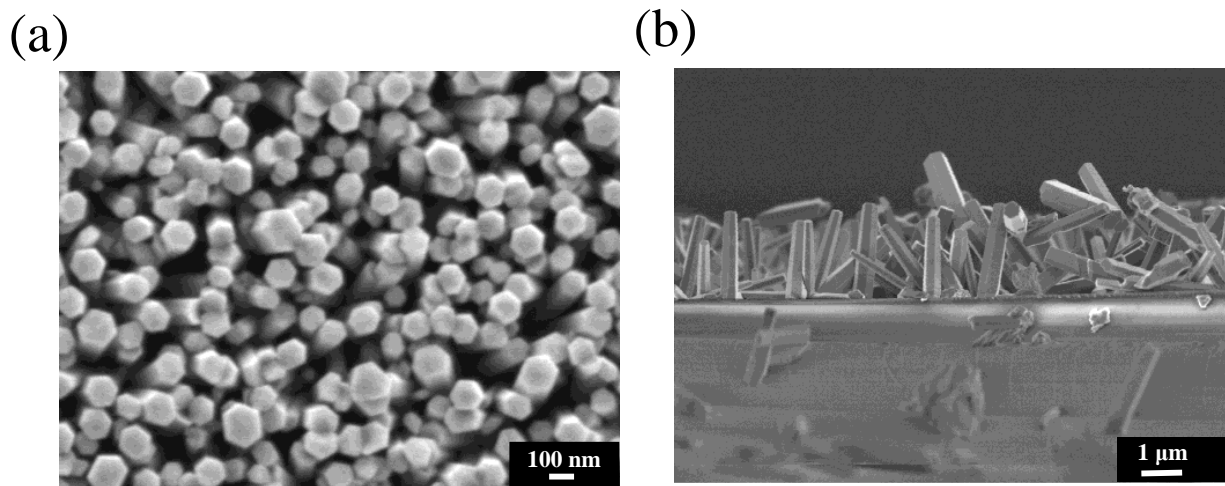


Figure 2. (a) Surface and (b) cross-sectional SEM image of ZnO nanorods on ITO-coated glass substrate.

Annealing at controlled temperatures in specific environments, such as nitrogen, is a well-established method for enhancing the stability and durability of nanostructures [38]. The high surface energy of freshly grown nanostructures often leads to their coalescence or degradation over time. Annealing allows for the relaxation of these high-energy surfaces, leading to more stable and robust structures. The annealing process can significantly impact the physical and chemical properties of the nanostructures [39]. It can enhance their crystallinity, reduce defects, and influence their electronic and optical characteristics, ultimately tailoring them for specific applications. For the CBD process of fabricating metal oxide semiconductors, post-treatment annealing is commonly adopted after the CBD process to improve the coating quality [40,41]. However, how the microstructures of metal oxide evolve under different annealing temperatures remains to be systematically investigated. In this work, the formation process of copper oxide on ZnO NRs under nitrogen and air annealing conditions was first explored by scanning electron microscopy (SEM). Previous studies have shown that appropriate annealing helps eliminate impurities, enhances crystallinity, and increases the grain size of copper oxide layers grown by CBD [42–44]. Here, we focus on elucidating the morphological evolution of copper oxide coatings by annealing over a temperature range of 100–400 $^{\circ}\text{C}$ under air or N_2 gas conditions. Additionally, post-annealing after CBD is necessary to stabilize the material structures before photoelectrochemical (PEC) testing in aqueous environments. The SEM images, as shown in Figure 3, indicate the formation process of copper oxide on ZnO NRs under N_2 gas annealing at different temperatures. Figure 3 (inset) shows the optical images of fabricated copper oxide/ZnO NRs under different annealing temperatures at N_2 gas. The yellow-to-orange color of films indicates the existence of Cu_2O [45]. The surface color of the grown Cu_2O thin films transitions from yellow to orange, with a more pronounced shift toward orange observed at higher annealing temperatures. At 100 $^{\circ}\text{C}$, we identified the presence of circular, fuzzy structures resembling fibers on the surface of the ZnO NRs. Upon increasing the temperature to 200 $^{\circ}\text{C}$, there was a discernible reduction in the abundance of these fiber-like features. At 300 $^{\circ}\text{C}$, the observation revealed the presence of tiny particulate Cu_2O on the surface of ZnO nanorods, indicating the effect of annealing at this temperature. As the temperature increased to 400 $^{\circ}\text{C}$, a hexagonal pattern of Cu_2O formed

on the ZnO NRs, suggesting a transformation in the structural arrangement of Cu_2O grains. The detailed SEM analysis provides valuable insights into the phase transition process of this composite material.

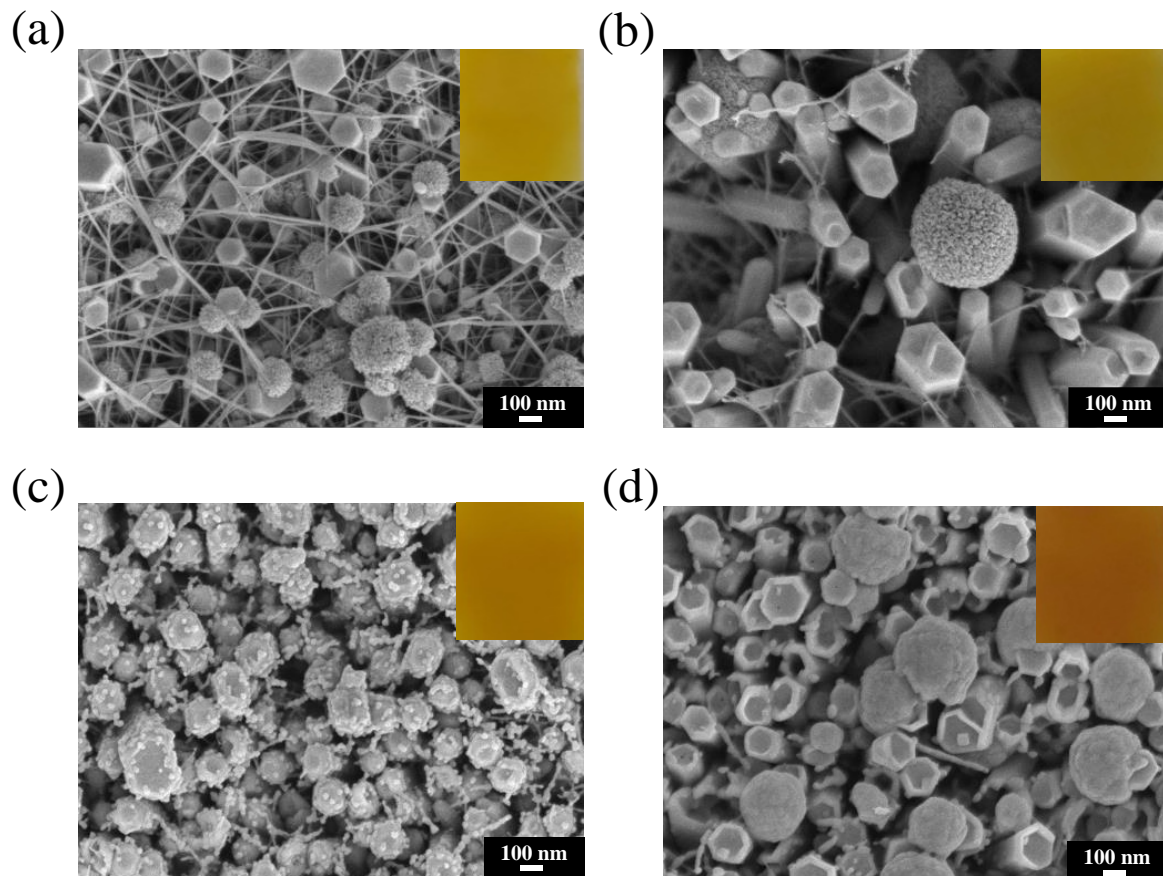


Figure 3. SEM surface morphologies and optical images (inset) of $\text{Cu}_2\text{O}/\text{ZnO}$ NR thin films treated under N_2 atmosphere at different annealing temperatures. (a) At lower temperatures, $100\text{ }^\circ\text{C}$, the formation of silk-like structures is observed, connecting the ZnO NRs. (b) With increasing temperature to $200\text{ }^\circ\text{C}$, the silk-like structures decrease. (c) At the annealing temperature of $300\text{ }^\circ\text{C}$, the fuzzy structures vanish, and small granular structures resembling Cu_2O form on the ZnO NRs. (d) At higher temperatures of $400\text{ }^\circ\text{C}$, the small granules arrange into hexagonal-like structures. The presence of the mushroom-shaped structures is noted in the samples annealed at $200\text{ }^\circ\text{C}$ and $400\text{ }^\circ\text{C}$.

The observed darkening of the samples annealed in air at $100\text{ }^\circ\text{C}$ to $400\text{ }^\circ\text{C}$, as shown in Figure 4 (inset), may be indicative of the formation of copper oxide (CuO). Copper oxide compounds are known to exhibit darker colors [46], and this color change suggests a chemical transformation during annealing. The presence of oxygen in the air during higher annealing temperatures could lead to the oxidation of copper species present on the surface or within the nanorods. The formation of CuO , which is thermodynamically favored under oxidative conditions under higher annealing temperatures, could account for the altered coloration of the samples. At elevated annealing temperatures (above $100\text{ }^\circ\text{C}$) in an air environment, we have observed the formation of interconnecting nanomaterials that bridge the gaps between individual ZnO NRs, as shown in Figure 4. These interconnecting materials give rise to a network-like structure that links the ZnO NRs together. Interestingly, the characteristic mushroom-like structures and granular aggregates, which were prevalent in samples annealed in N_2 , were notably absent in samples annealed in air at higher temperatures. This disparity raises questions about the underlying mechanisms responsible for the differences in nanostructure growth under varying annealing conditions. We postulate that the interconnecting nanomaterials observed in air annealing may result from

the oxidation of ZnO NRs in the presence of atmospheric oxygen. The increased annealing temperature may enhance the reactivity of the system, leading to the formation of these interconnecting materials. The presence of interconnecting nanomaterials and the absence of mushroom-like structures and granular aggregates suggest that the ambient conditions and annealing temperature play a crucial role in determining the final morphology and properties of the nanostructures. Additionally, the observed increase in the diameter of the ZnO NRs, particularly with elevated annealing temperatures, can be attributed to the copper oxide precursor acting as nucleation sites or catalysts, influencing the growth of ZnO NRs. The presence of the precursor material could lead to the formation of new nuclei on the surface of the nanorods, contributing to an increase in diameter. Moreover, the diffusion and potential alloying between copper and zinc during annealing may play a significant role. The high-temperature annealing process could facilitate the diffusion of copper into the zinc oxide nanorods, potentially leading to changes in their crystal structure and dimensions.

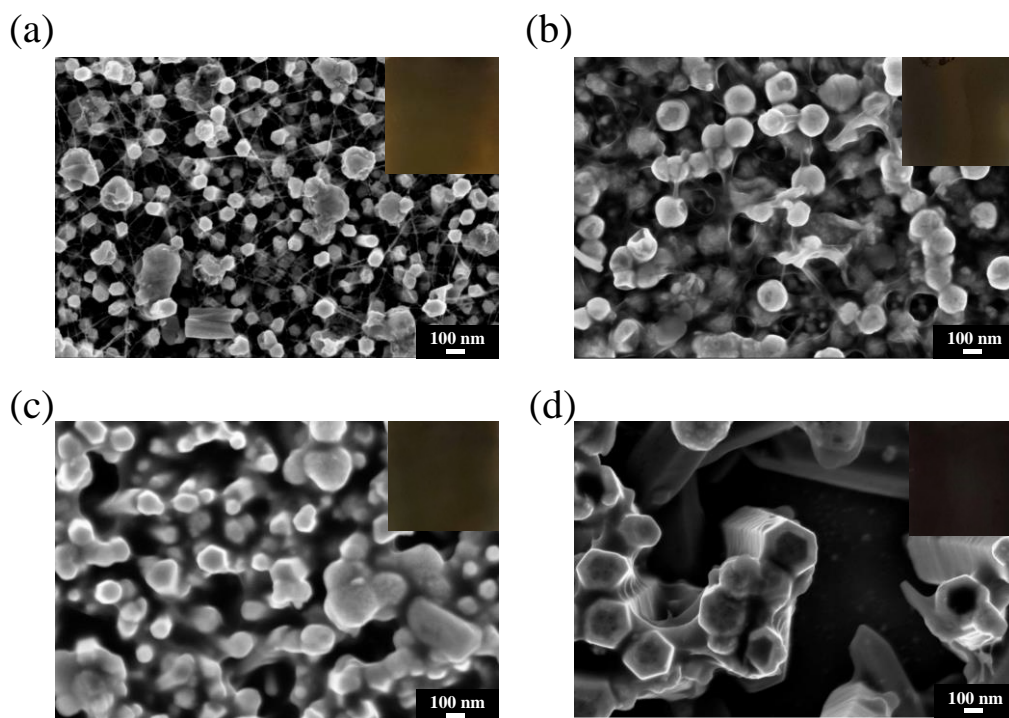


Figure 4. SEM surface morphologies and optical images of CuO/ZnO NR thin films treated under ambient air atmosphere at different annealing temperatures. (a) At 100 °C, the presence of fewer silk-like structures compared to the N₂ atmosphere is observed. (b) Annealing at 200 °C results in the reduction of silk-like structures, while (c) at 300 °C, the fuzzy structures gradually disappear, and network-like structure of CuO links the ZnO NRs together. (d) At 400 °C, the small granules form hexagonal-like structures, similar to the nitrogen atmosphere. The absence of mushroom-shaped structures is noted in all samples annealed in ambient air.

SEM coupled with energy-dispersive X-ray spectroscopy (SEM-EDS) analysis revealed a distinctive spatial distribution of Cu, O, and Zn atoms, as shown in Figure 5. Figure 5 also displays a representative SEM image with EDS analysis showing the atomic concentration of each element. Copper atoms (Cu) are represented in red, oxygen atoms (O) in blue, and zinc atoms (Zn) in green. The atomic composition of the sample was determined to be approximately 54.2:15.3:30.5 (O:Cu:Zn). A finding is the preferential enrichment of Cu atoms at the tips of the nanorods forming distinct red regions in the elemental map. This observation indicates that during air annealing, CuO exhibits a strong affinity for nucleation and growth at the apex of the ZnO NRs.

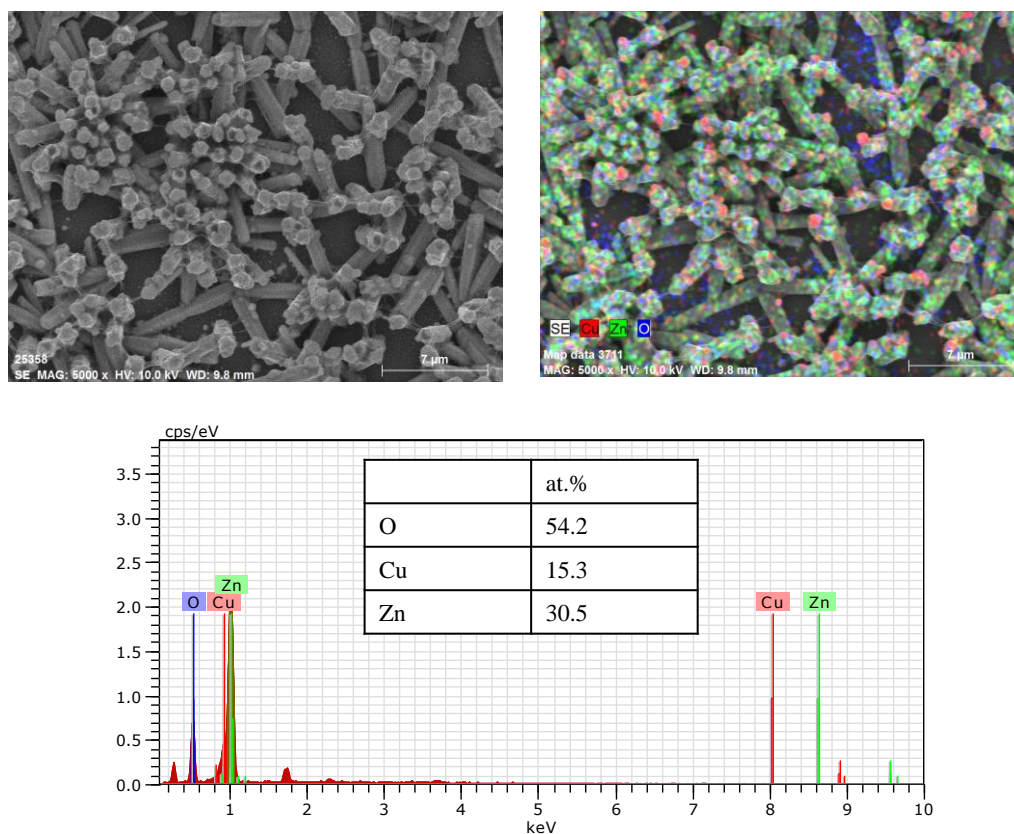


Figure 5. SEM-EDS analysis of CuO-coated ZnO NRs. The sample was annealed in ambient air at 200 °C.

Figure 6 shows the absorption spectra of copper-coated ZnO NRs fabricated under N_2 and air annealing conditions at different temperatures. In the case of copper-coated ZnO NR samples annealed under N_2 gas (samples show yellow color), we observed a significant increase in absorbance within the wavelength range of 450 nm to 700 nm as the annealing temperature increased to 200 °C, as shown in Figure 6a. This increase suggests that a structural or compositional change has occurred at lower annealing temperatures, resulting in improved absorbance of visible light. However, with a further increase in annealing temperature (400 °C), the absorbance of the samples in the visible light range did not continue to rise, and there was a decrease in absorbance in the wavelength range of 400 nm to 500 nm. In the case of copper-coated ZnO NRs annealed under ambient air (samples showing dark brown color), an interesting optical behavior was observed with increasing annealing temperature. Specifically, as the annealing temperature reached 200 °C, there was a noticeable increase in absorbance within the wavelength range of 450 nm to 700 nm, as shown in Figure 6b. This increase in absorbance was more pronounced compared to samples annealed under N_2 gas, particularly within the visible light wavelength range. Moreover, the enhancement in absorbance within the visible light spectrum continued as the annealing temperature further increased. Remarkably, the sample annealed at 400 °C exhibited absorbance characteristics, making it the most efficient in terms of visible light absorption. Tauc plot analyses, as shown in Figure 6c,d, revealed distinct trends in the bandgap (E_g) of copper-oxide-coated ZnO thin films annealed in N_2 and air atmospheres. For samples annealed in a N_2 environment, the bandgap ranged between 2.35 eV and 2.5 eV within the 100 °C to 400 °C annealing temperature range. In contrast, thin films annealed in air exhibited bandgaps in the range of 1.8 eV to 2.25 eV. Notably, the bandgap of samples annealed in air was found to be at its minimum, especially the sample annealed at 400 °C, suggesting enhanced absorption of visible light.

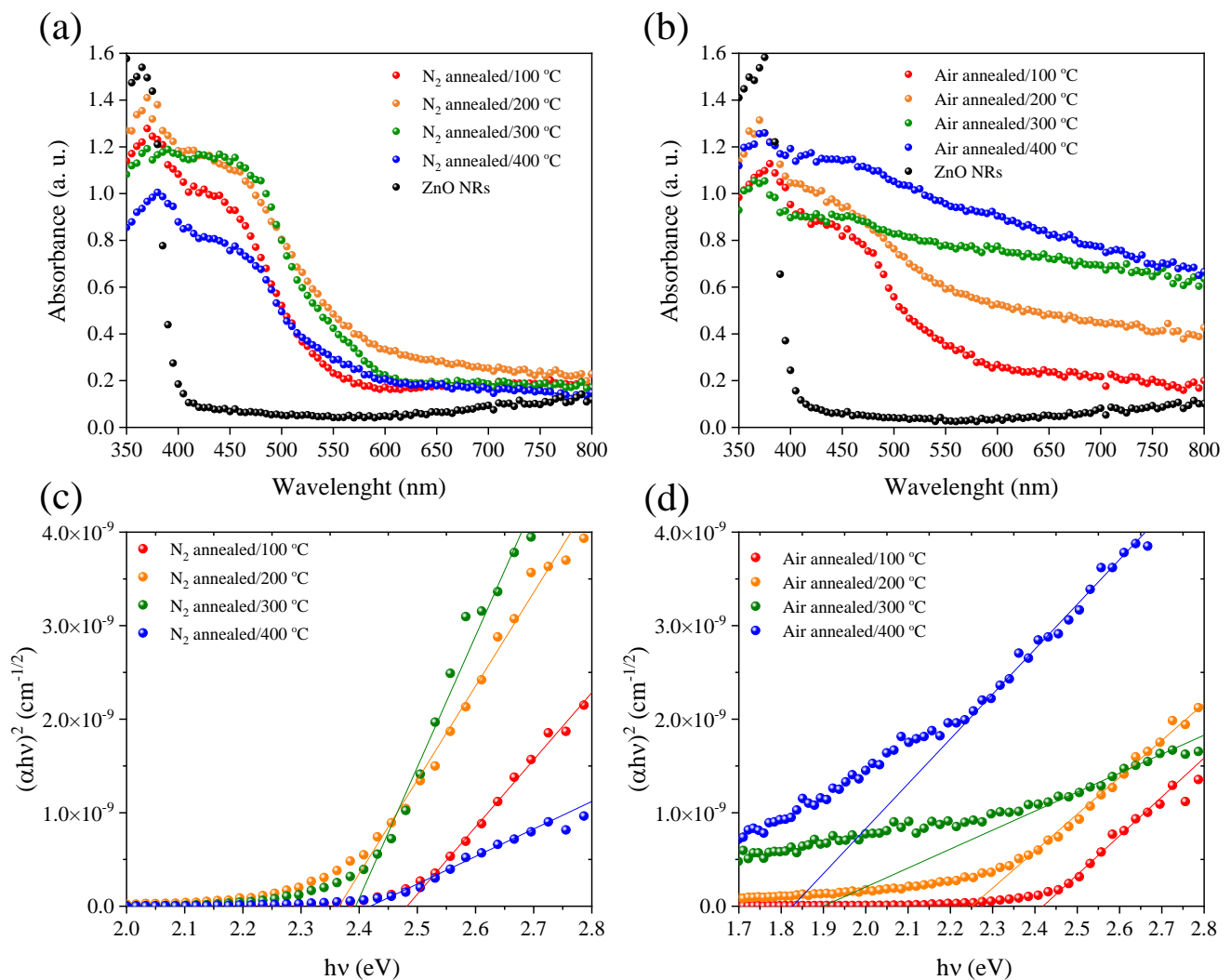


Figure 6. Comparative absorbance spectra of copper-oxide-coated ZnO NRs annealed under (a) N_2 gas atmosphere and (b) ambient air. The corresponding Tauc plot of copper-oxide-coated ZnO NRs annealed under (c) N_2 gas atmosphere and (d) ambient air. The copper-coated ZnO NRs annealed above $300\text{ }^\circ\text{C}$ under air condition show significantly enhanced absorbance within the visible light range and reduced bandgap energy compared to samples annealed under N_2 gas, indicating improved visible light absorption properties.

3.2. XRD Analysis Revealing the Influence of Cu_2O and CuO on Structural Evolution and Preferred Orientation in ZnO Nanorods

Figure 7 compares the XRD pattern of different samples, ZnO NRs, copper oxide annealed at $200\text{ }^\circ\text{C}$ under N_2 gas, copper-oxide-coated ZnO NRs annealed at $200\text{ }^\circ\text{C}$ under N_2 gas, and copper oxide annealed at $400\text{ }^\circ\text{C}$ under ambient air. All the samples show a strong characteristic peak of a (002) plane at $2\theta \approx 34.2^\circ$, indicating the formation of ZnO NRs [47]. A weak peak at around $2\theta \approx 36.5^\circ$ corresponds to the presence of a (111) plane indicating pure cuprous oxide (Cu_2O) [48], both shown in the pure Cu_2O - and Cu_2O -coated ZnO NR samples. Weak peak at around $2\theta \approx 38.5^\circ$ corresponds to the presence of (111) plane indicating pure cupric oxide (CuO) [49], only shown in the CuO -coated ZnO NR sample.

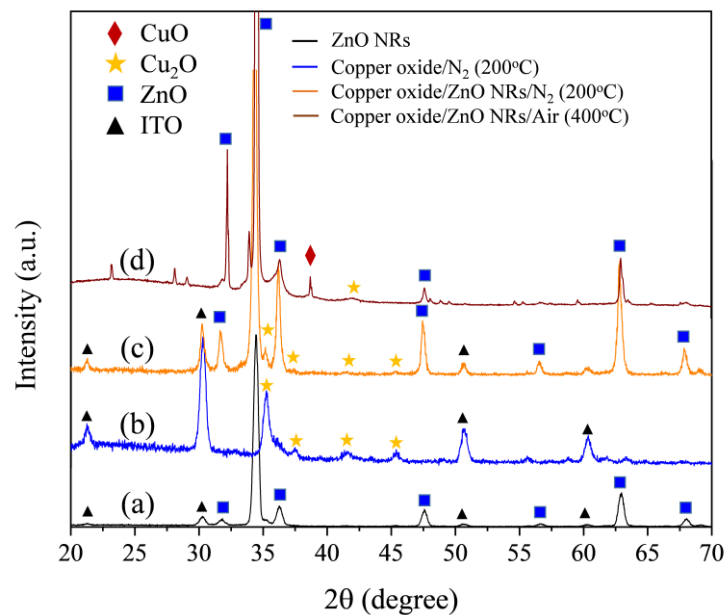


Figure 7. X-ray diffraction (XRD) patterns of (a) pure ZnO NRs, (b) pure Cu_2O , and (c) Cu_2O grown on ZnO NRs. Those three samples were annealed at 200 °C under N_2 gas environment. (d) XRD pattern of CuO grown on ZnO NRs, annealed at 400 °C under air condition.

The XRD pattern of ZnO NRs typically shows an enhanced intensity of the (002) diffraction peak, indicating the nanorods grow preferentially along the (001) direction. However, in this work, the (002) peak intensity was found to decrease with increasing N_2 gas annealing temperature when Cu_2O was modified on the surface of ZnO NRs, as shown in Figure 8a. Several factors may account for the reduced preferential orientation after annealing. The migration of Cu_2O during thermal treatment disrupts the original structure of ZnO nanorods, leading to a weaker (002) preferred growth. Recrystallization of ZnO occurs upon annealing, with increased growth rates along certain directions at the expense of preferred orientation. The annealing process likely compromises the structure and morphology of ZnO NRs, resulting in the reduced intensity of the (002) reflection in the XRD pattern. Figure 8b shows the (002) diffraction peak of ZnO NRs in the XRD pattern became sharper and slightly shifted after annealing the copper-oxide-coated ZnO NRs heterostructure in ambient air. The sharpening of the (002) peak can be ascribed to the improved crystallinity of ZnO during annealing, which reduces the defects and enhances the reflection from the (002) plane. The oxygen atmosphere may also facilitate the preferred orientation of ZnO along the (001) direction, further strengthening the (002) diffraction. Additionally, the modification of CuO could inhibit the growth of other orientations in ZnO, making the relative intensity of the (002) reflection more pronounced. The thermal treatment may also introduce stress that leads to minor changes in peak positions. Moreover, the modification of CuO could vary the defect density on the surface of ZnO NRs, influencing the microscopic strain [50]. The oxygen annealing improves the crystallinity and preferred orientation of ZnO NRs, while the modification of CuO promotes the relative intensity of the (002) reflection, collectively resulting in a sharper (002) XRD peak. Meanwhile, effects like solid solubility and stress during thermal treatment induce slight peak shifts.

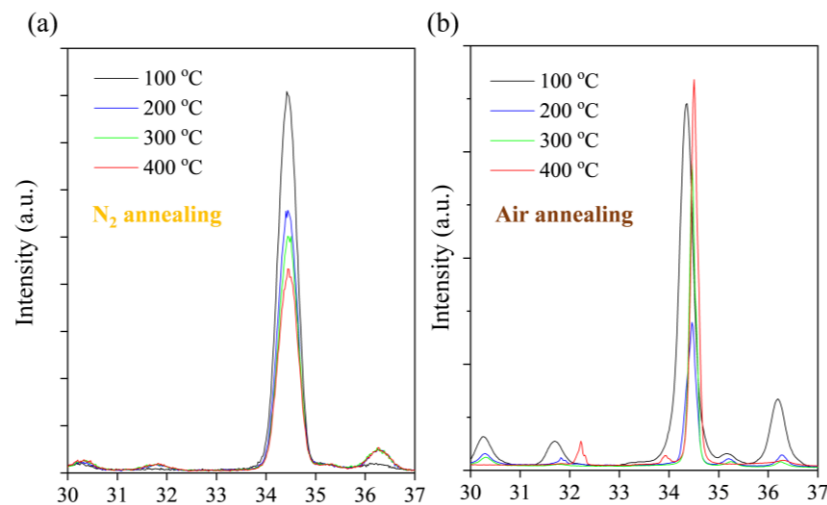


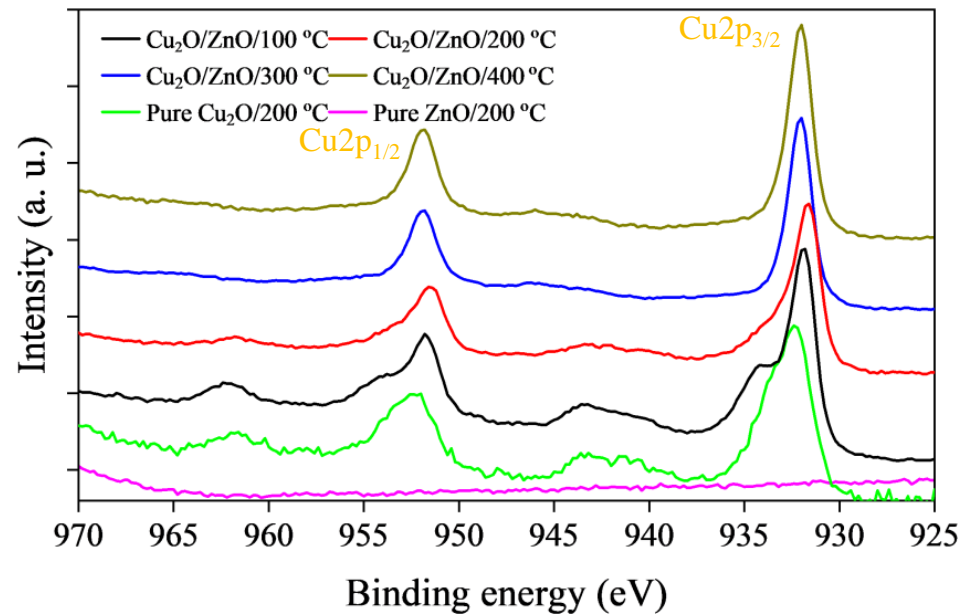
Figure 8. X-ray diffraction (XRD) patterns of copper-oxide-coated ZnO NRs under (a) N₂ gas and (b) ambient air annealing at different temperatures.

3.3. Investigation of Binding Energy Shifts in O1s, Cu 2p_{3/2}, and Zn 2p_{3/2} Core Levels

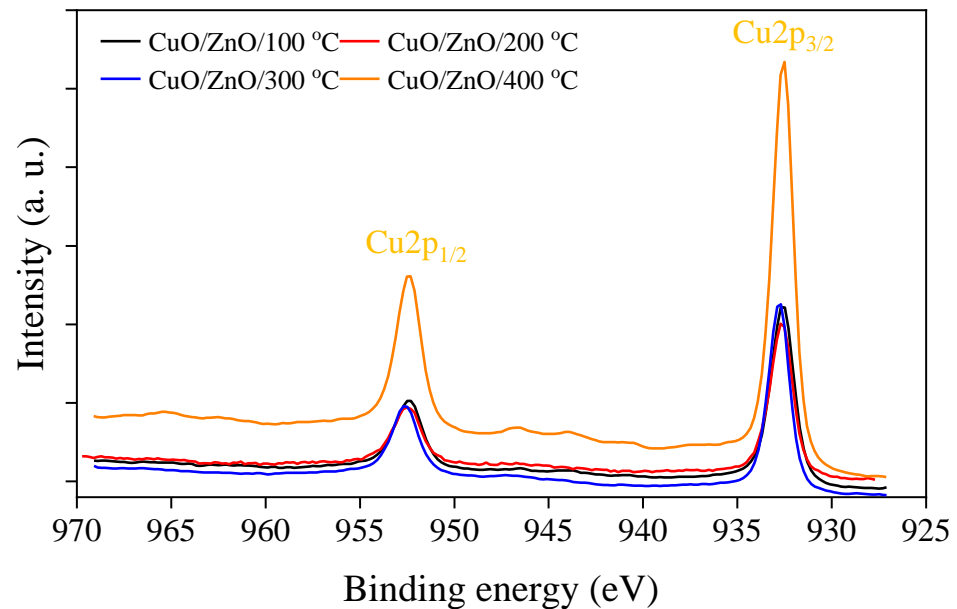
In our investigation, we performed X-ray photoelectron spectroscopy (XPS) on copper oxide grown on ZnO NRs fabricated by varying annealing temperatures corresponding to N₂ gas or ambient air. We observed a distinctive behavior in the Cu2p_{3/2} binding energy for samples under N₂ gas annealing at different temperatures, as shown in Figure 9a. As the annealing temperature increased, we noted a significant downward shift in the Cu2p_{3/2} binding energy when compared to the pure Cu₂O reference. This observed shift is intriguing and suggests an interaction between Cu₂O and ZnO during the annealing process. We also observed a shoulder located at the high binding energy (934 eV) of the main peaks in the 100 °C-annealed sample. This shoulder gradually disappeared as the annealing temperature increased. The location of the shoulder might be due to the generation of a CuO phase, which disappeared at higher temperatures under N₂ gas annealing conditions. The observed energy shift of Cu2p_{3/2} binding energy is consistent with the development of interfacial electronic states at the Cu₂O-ZnO interface. This effect is likely due to charge transfer and electronic restructuring between Cu₂O and ZnO, impacting the final electronic structure and thus causing a binding energy shift in the XPS spectra [51]. In contrast, for CuO-coated ZnO nanorods, the Cu2p_{3/2} binding energy remained relatively unaffected by variations in the annealing temperature, as shown in Figure 9b. This lack of a significant shift implies that the CuO-ZnO interaction differs from that of Cu₂O-ZnO. CuO has a different electronic structure compared to Cu₂O, and it does not exhibit the same extent of interaction with ZnO, leading to a consistent Cu2p_{3/2} binding energy [52].

Figure 10 shows the Zn2p_{3/2} binding energy of the copper-oxide-coated ZnO NRs under different annealing conditions. For Cu₂O-coated ZnO NRs, we noted a notable shift in the Zn2p_{3/2} binding energy towards higher binding energies as the annealing temperature increased. In contrast, the Zn2p_{3/2} binding energy for CuO-coated ZnO NRs remained relatively unaffected by changes in annealing temperature. The observed shift in the Zn2p_{3/2} binding energy for Cu₂O-coated ZnO nanorods suggests a change in the chemical environment of zinc ions within the nanocomposite. This shift towards higher binding energies indicates an increase in the energy required to remove electrons from Zn 2p orbitals, which can be attributed to alterations in the local electronic structure. One possible explanation is the formation of new chemical bonds or changes in coordination environments around Zn ions due to the interaction with Cu₂O and annealing. This change in the chemical environment is consistent with the previously observed shift in Cu2p_{3/2} binding energy, reinforcing the idea of complex electronic interactions between Cu₂O and ZnO. Conversely, the consistent Zn2p_{3/2} binding energy for CuO-coated ZnO NRs under varying annealing temperatures implies a stable chemical environment around

the Zn ions. The lack of binding energy shifts indicates that CuO interacts differently with ZnO, maintaining a more uniform electronic structure. The difference in Zn2p_{3/2} binding energy shifts between Cu₂O-coated and CuO-coated ZnO NRs further highlights the distinct interactions of these oxide materials with ZnO. These findings suggest that Cu₂O can influence the electronic structure of ZnO in a manner that is sensitive to annealing conditions, resulting in binding energy shifts for both Cu and Zn elements. On the other hand, CuO maintains a relatively constant electronic environment within the composite, demonstrating its distinct behavior.



(a)



(b)

Figure 9. XPS spectra of copper-oxide-coated ZnO NRs under (a) N₂ gas and (b) ambient air annealing at different temperatures.

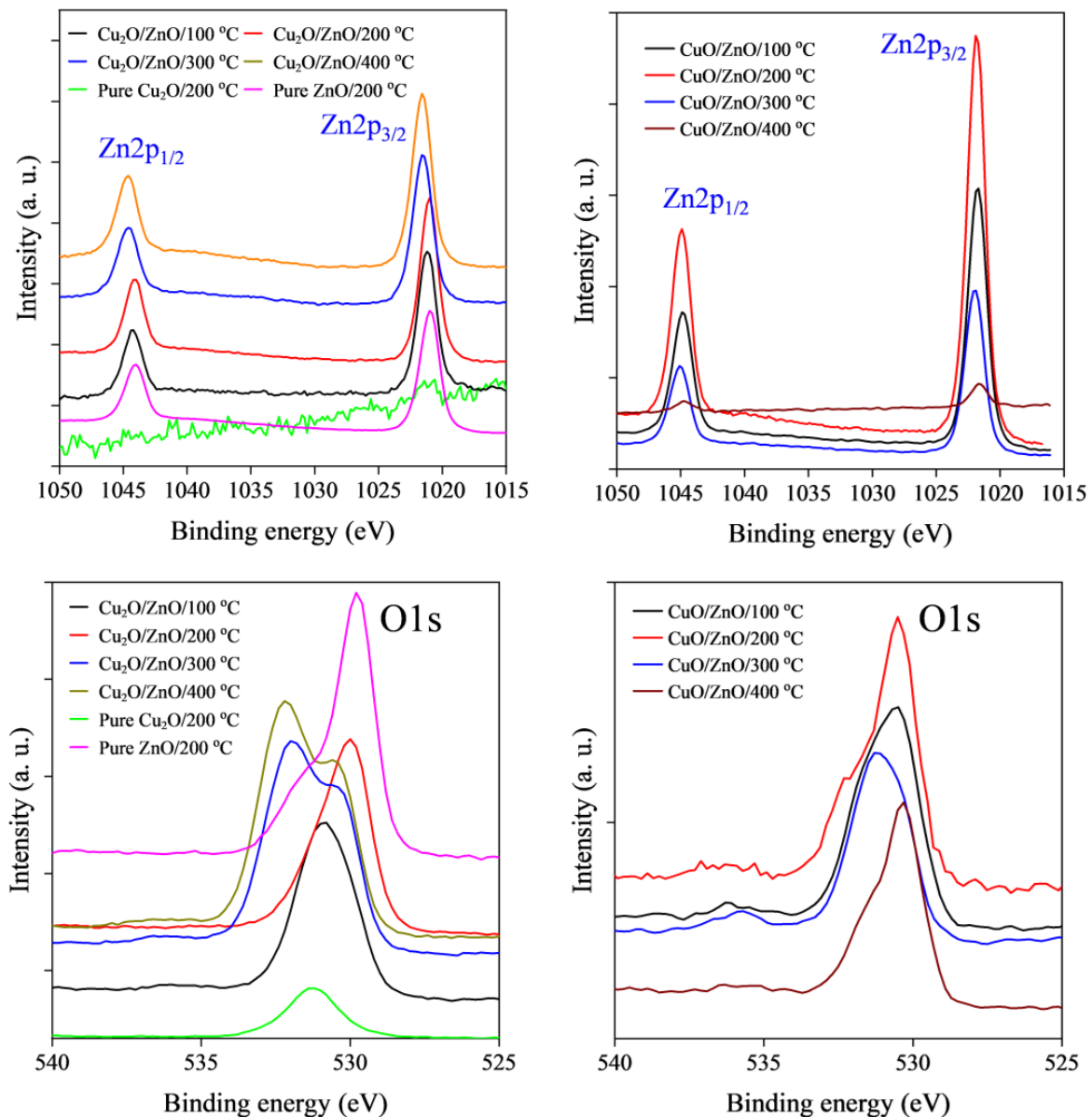


Figure 10. XPS spectra of Cu_2O -ZnO NRs and CuO-ZnO NRs fabricated by different annealing temperatures and atmospheric conditions.

Figure 10 also shows the O1s XPS binding energy observed in the Cu_2O -coated ZnO and CuO-coated ZnO NRs under different annealing temperatures. The observed O1s XPS binding energy shifts in Cu_2O -coated ZnO NRs are indeed intriguing. The shift towards higher binding energy for the major peak (from 532 eV to 533 eV) indicates changes in the oxygen chemical environment within the Cu_2O -ZnO nanocomposite. The O1s binding energy in pure ZnO nanorods is typically observed around 530 eV. This position is consistent with oxygen atoms in the ZnO lattice, which are part of the oxide structure of the nanorods. In pure Cu_2O , the O1s binding energy is observed to be around 532 eV. This is expected as Cu_2O is a compound consisting of copper and oxygen atoms, and the O1s peak represents oxygen in the Cu_2O crystal structure. The shift in the O1s binding energy to a higher energy state (533 eV) when Cu_2O is coated on ZnO nanorods after annealing is indicative of changes in the local chemical environment of oxygen. This shift may be attributed to the interaction between Cu_2O and ZnO during annealing, leading to the formation of new chemical bonds and compounds. The oxygen atoms near the interface between Cu_2O and ZnO may experience altered chemical environments, resulting in a higher binding energy

state. Another possible reason for the shifting is the formation of oxygen vacancies or defects when the Cu₂O-ZnO NRs were annealed at N₂ gas. The annealing process could also result in changes in the O1s binding energy. These defects can introduce new energy states in the XPS spectrum [53]. The absence of a significant shift in the O1s binding energy for CuO-coated ZnO NRs under ambient air annealing conditions suggests differences in the chemical behavior of CuO compared to Cu₂O when interfaced with ZnO. CuO and Cu₂O are different copper oxide phases with distinct chemical properties. When interfaced with ZnO, they may form different chemical bonds and structures. The chemical interactions between CuO and ZnO may not induce the same shifts in O1s binding energy as those observed in the Cu₂O-coated sample since Cu₂O is a p-type semiconductor with copper-deficient oxygen stoichiometry, whereas CuO is an n-type semiconductor with stoichiometric oxygen. The different oxygen stoichiometries could lead to distinct oxygen vacancy formation and charge transfer processes at the interface. These differences can affect the O1s binding energy. Also, CuO and Cu₂O have different crystal structures, which can influence the nature of their interfaces with ZnO. Crystal defects, grain boundaries, and interfacial structures play a role in determining XPS binding energies.

3.4. Electrochemical and Photoelectrochemical(PEC) Measurement of Cu₂O- and CuO-Coated ZnO Nanorods Fabricated Using Different Annealing Conditions

Studying the cyclic voltammetry (CV) of nanomaterials while observing before and after exposure to light holds great significance and importance in the realm of materials science and electrochemistry. Specifically, when nanomaterials are subjected to light irradiation, distinct changes in the CV curves become evident, characterized by a noticeable increase in current and a pronounced shift towards the positive potential range. These changes signify the effective conversion of incident light energy into electrical current, indicative of the material's efficient light absorption and photoinduced electron-hole pair generation. The anodic peaks in the CV curve correspond to oxidation reactions, typically representing the transfer of photogenerated electrons. A stronger anodic peak suggests efficient electron-hole pair generation and their effective involvement in electrochemical reactions. Conversely, the cathodic peaks, representative of reduction reactions, reveal insights into the recombination of photogenerated electron-hole pairs. A weaker cathodic peak implies reduced recombination, contributing to the preservation of the long-lived electron-hole pairs and enhanced photocatalytic efficiency. The potential difference between the anodic and cathodic peaks within the CV curve is another critical parameter. A larger potential difference typically indicates the material's ability to generate photogenerated electron-hole pairs at lower energy excitation levels, which is of paramount importance in photoredox and energy conversion applications. Figure 11 shows the photoelectrochemical (PEC) behavior of ZnO nanorods and ZnO/Cu₂O heterostructures prepared by varying the number of chemical bath deposition (CBD) cycles. CV measurements were conducted to assess the impact of visible light irradiation on the electrochemical response of the materials. CV measurements of pristine ZnO nanorods before and after light exposure revealed minimal changes in the electrochemical response. This suggests that ZnO nanorods alone exhibit limited photoresponse to visible light [54]. The CV curves of ZnO/Cu₂O heterostructures with five CBD cycles displayed pronounced increases in current and anodic peak intensity after light exposure. These observations indicate enhanced photoconversion efficiency, likely attributed to improved light absorption and efficient charge separation within the heterostructure. Similar to the heterostructures with 5 CBD cycles, those with 10 CBD cycles exhibited enhanced photoresponse. The CV curves displayed increased current and anodic peak intensity upon visible light irradiation, underscoring the improved photoelectrochemical properties. Intriguingly, the ZnO/Cu₂O heterostructure with 15 CBD cycles demonstrated a distinct enhancement in the cathodic peak of the CV curve after light irradiation. This suggests a different electron transfer behavior within the heterostructure, which may be attributed to the unique properties introduced by the increased number of Cu₂O layers.

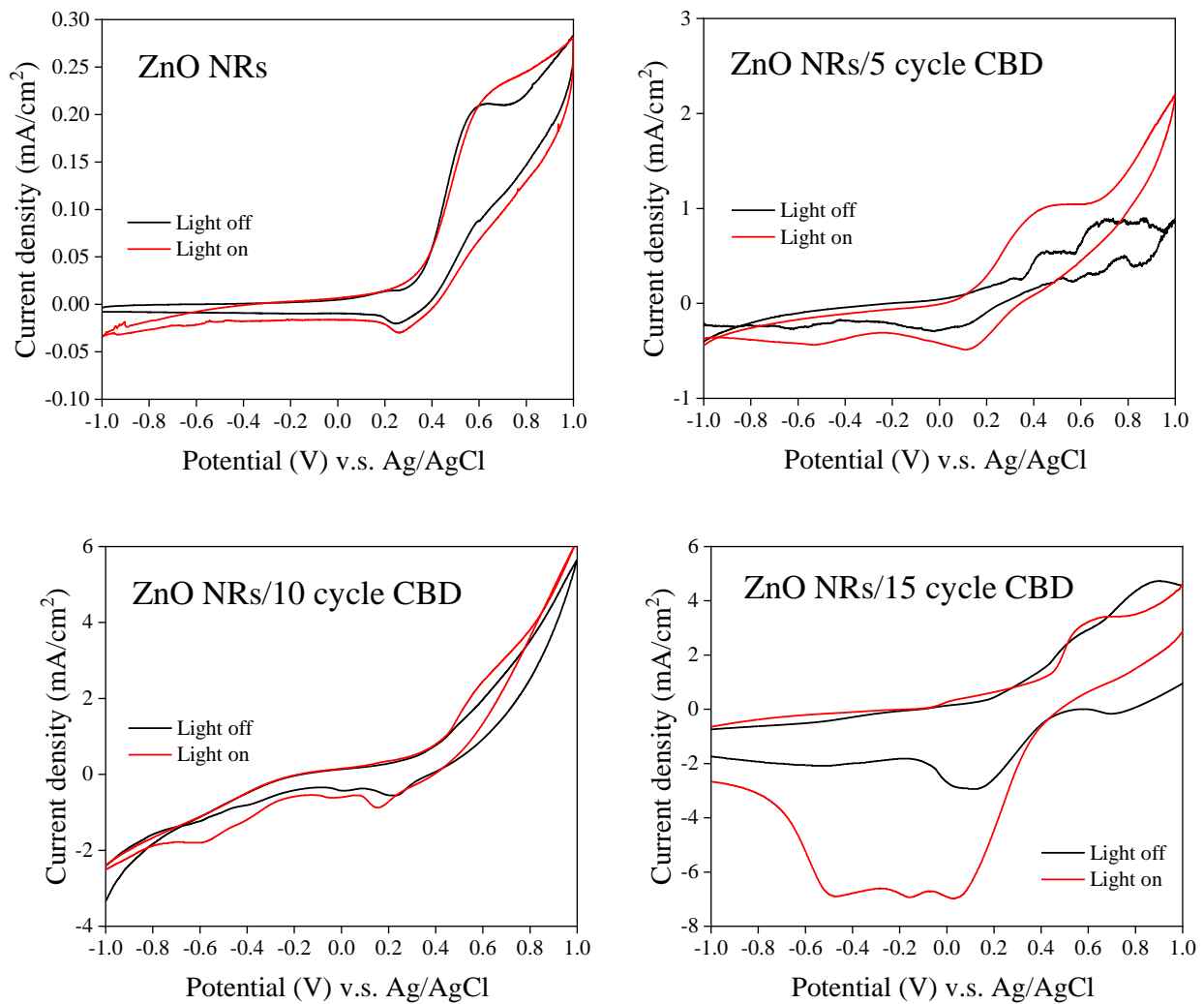


Figure 11. Cyclic voltammetry (CV) curves of ZnO nanorods and ZnO/Cu₂O heterostructures before (black lines) and after (red lines) visible light exposure. Pristine ZnO nanorods showing minimal changes in photoresponse; ZnO/Cu₂O heterostructures with 5 CBD cycles, demonstrating significant increases in current and anodic peak intensity after light exposure; ZnO/Cu₂O heterostructures with 10 CBD cycles, exhibiting enhanced photoresponse similar to heterostructures with 5 CBD cycles; ZnO/Cu₂O heterostructures with 15 CBD cycles, where a distinct enhancement in cathodic peak intensity is observed after light irradiation.

Figure 12 shows the PEC performance of Cu₂O-coated Zn NRs fabricated by different annealing temperatures before and under white light illumination. When applying a positive bias, all samples exhibit similar dark current and photocurrent behaviors. However, notable differences arise when a negative bias is applied. At a bias of -0.4 V, distinct variations in photocurrent and dark current are observed among the samples annealed at 100 °C, 200 °C, 300 °C, and 400 °C. The photocurrent and dark current diverge significantly as the annealing temperature varies. Specifically, at -0.4 V bias, the photocurrent-to-dark current increments for the samples annealed at 100 °C, 200 °C, 300 °C, and 400 °C are 0.25 , 1.5 , 1.7 , and 2.0 mA/cm², respectively. This observation suggests that the annealing process, particularly at temperatures of 200 °C and above, significantly influences the PEC performance of the Cu₂O-coated ZnO NRs. The annealing temperature has a significant impact on the morphology and PEC performance of Cu₂O-ZnO nanocomposites. SEM images revealed the morphological evolution of Cu₂O on ZnO nanorods during annealing. We observed a substantial improvement in both the dark current and photocurrent of the samples when annealed at 200 °C, which may be attributed to the specific morphological

changes in Cu_2O . At this temperature, Cu_2O begins to form larger, more ordered structures, enhancing the electrochemical performance of the samples. A significant improvement in both the dark current and photocurrent in the PEC measurements observed in the Cu_2O -coated ZnO NRs could also be correlated to the XRD and XPS results. The XRD results suggested that annealing at $200\text{ }^\circ\text{C}$ helps to enhance the crystallinity of ZnO NRs. The improved crystal quality might lead to better charge transport and separation, both of which are crucial for efficient photocatalytic activity. The XPS findings revealed changes in the electronic structure at the Cu_2O -ZnO interface. This alteration in electronic structure likely plays a role in the observed improvement in PEC performance. The reconfiguration of electronic states may facilitate more efficient charge transfer and separation, leading to enhanced photocurrent [33]. However, as the annealing temperature continues to increase, there is no further significant improvement in the performance of dark current and photocurrent. This could be because Cu_2O has already reached its optimal morphology and crystalline state at $200\text{ }^\circ\text{C}$, and further temperature increase offers limited performance enhancement. These observations suggest that by carefully controlling the annealing temperature, the morphology and electrochemical performance of Cu_2O -ZnO nanocomposites can be tailored.

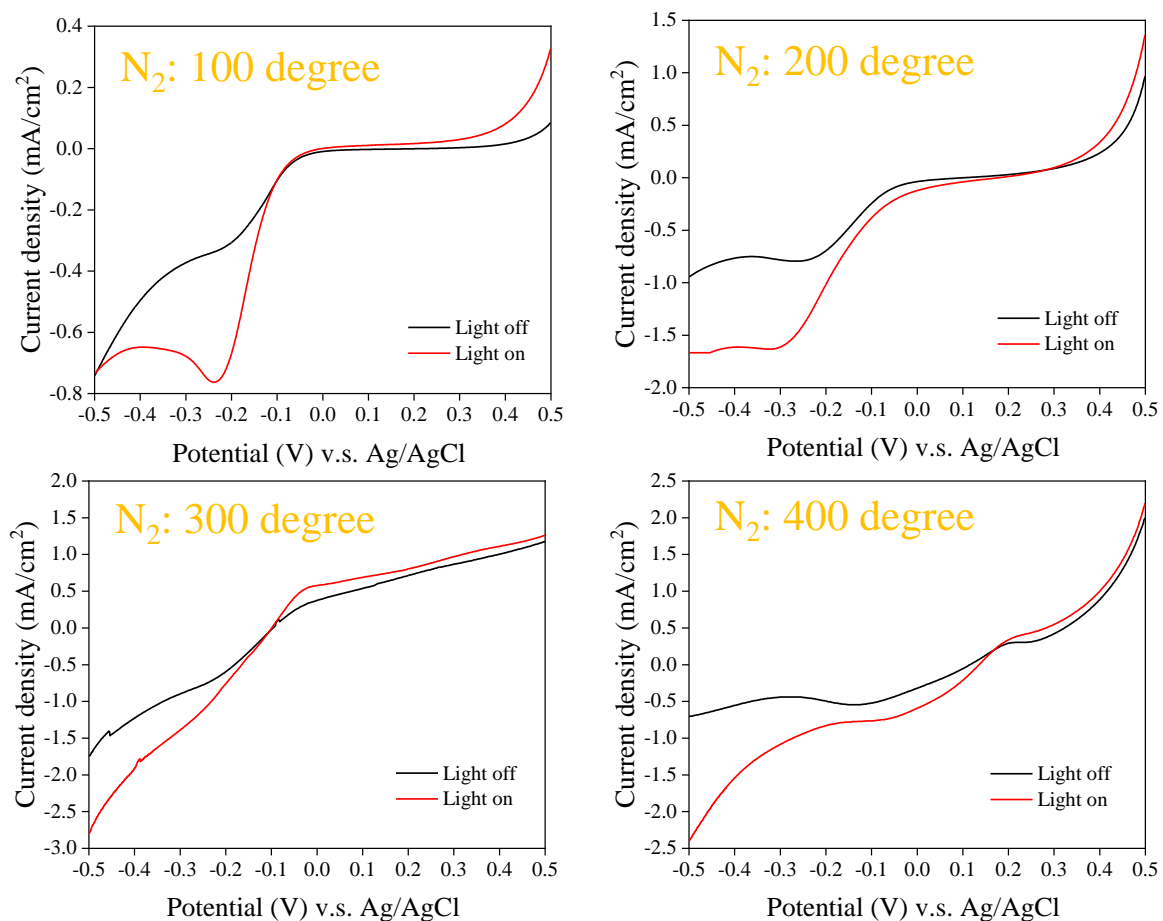


Figure 12. Dark current and photocurrent density analysis of Cu_2O -coated ZnO nanorods fabricated using different annealing temperatures under N_2 gas conditions.

When applying a positive bias, all Cu_2O -coated ZnO NR samples exhibit similar dark current and photocurrent characteristics, as shown in Figure 13. However, distinctive differences emerge when a negative bias is applied. At a bias of -0.4 V , a significant variance in photocurrent and dark current is observed among the samples. Specifically, at -0.4 V bias, the photocurrent-to-dark current increments for the Cu_2O -coated ZnO NRs annealed at $100\text{ }^\circ\text{C}$, $200\text{ }^\circ\text{C}$, $300\text{ }^\circ\text{C}$, and $400\text{ }^\circ\text{C}$ are 0.35 , 0.7 , 2.8 , and 10.0 mA/cm^2 , re-

spectively. These results highlight the substantial impact of annealing temperature on the photoelectrochemical properties of the CuO-coated ZnO nanorods under negative bias conditions. The remarkable increase in photocurrent-to-dark current incensement as a function of annealing temperature, especially at 400 °C, reflects a notable enhancement in the material's ability to generate photocurrent when subjected to negative bias. The variations in PEC performance, particularly the differences in dark current and photocurrent at -0.4 V bias, show a clear trend. The sample annealed at 400 °C exhibits the most substantial difference of 10.0 mA/cm^2 , while the 100 °C annealed sample shows the smallest difference of 0.35 mA/cm^2 . This trend suggests that the morphological changes observed in the SEM images could be closely related to the differences in PEC performance. The interconnecting nanomaterials formed in air annealing may offer enhanced charge transport pathways and surface area for improved PEC performance compared to the N_2 -annealed samples. The enhanced crystallinity and peak intensities seen in the XRD pattern at higher annealing temperatures align well with the observed increase in the light-to-dark current difference. Improved crystallinity typically indicates fewer crystal defects and enhanced charge carrier mobility, contributing to better PEC performance. The shifts in peak positions may be related to structural modifications, such as changes in grain size and orientation, which can directly affect the electronic properties and charge transport within the CuO and ZnO NRs. Furthermore, the appearance of new peaks or altered peak positions in the XRD pattern observed in CuO-coated ZnO NRs may indicate phase transformations or changes in the crystal structure. These structural modifications can influence the band structure and surface states, which, in turn, affect the PEC behavior.

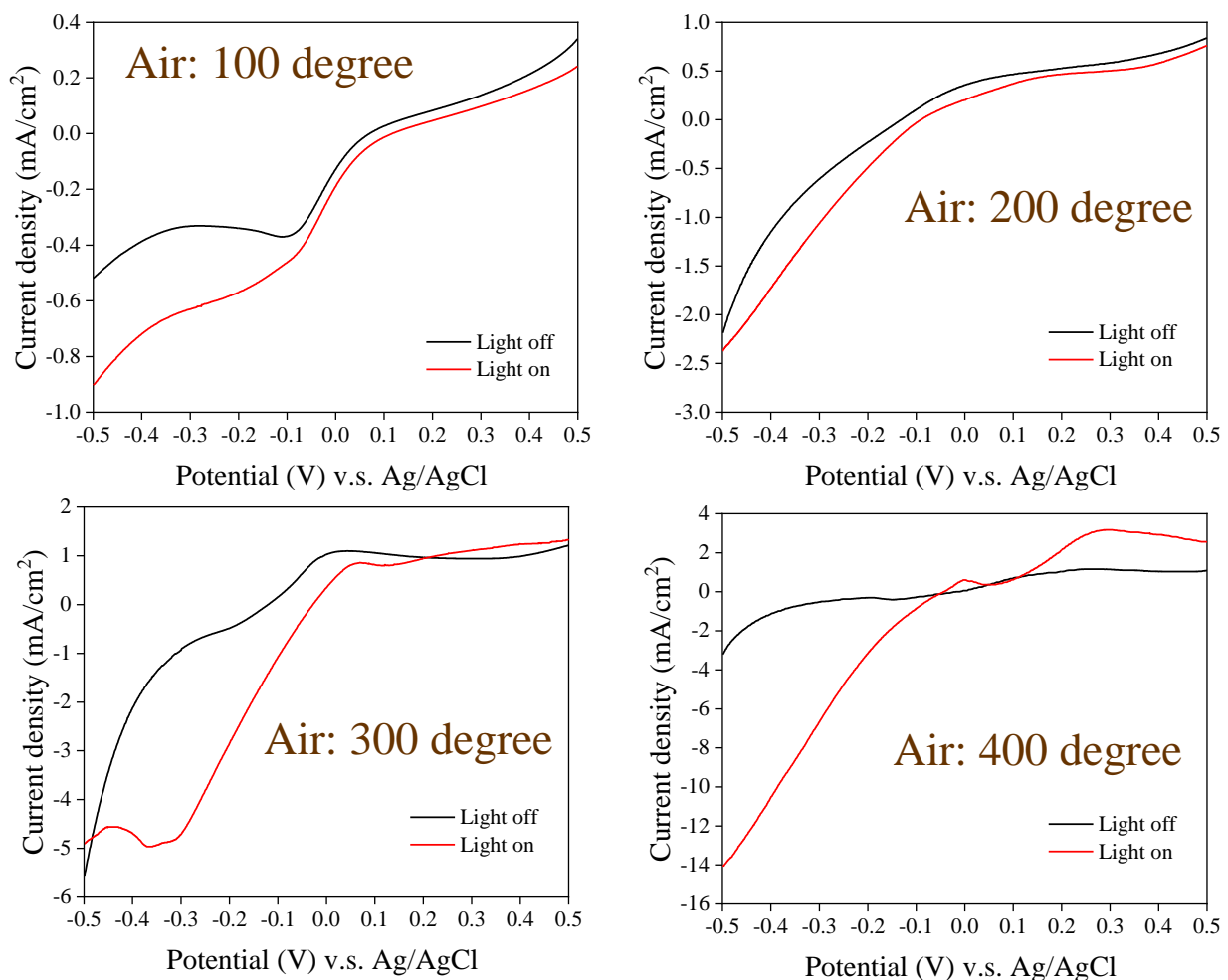


Figure 13. Dark current and photocurrent density analysis of CuO-coated ZnO nanorods fabricated using different annealing temperatures under ambient air conditions.

In our study, we observed a remarkable difference in the PEC behavior between CuO-coated ZnO NRs and Cu₂O-coated ZnO NRs, with CuO-coated samples exhibiting superior performance. This enhancement can be attributed to several key factors. CuO has a more favorable band structure compared to Cu₂O. The conduction band of CuO is lower in energy, allowing for more efficient electron transfer to the electrode. This is crucial for enhancing the photocurrent in PEC cells. CuO-coated ZnO NRs exhibit improved charge carrier separation and reduced recombination rates [32]. This results in a higher photocurrent, as more photogenerated electrons and holes reach the electrode instead of recombining. The morphology of CuO coatings on ZnO nanorods can provide a higher surface area, which promotes more active sites for photochemical reactions. This increased surface area can lead to higher photocurrent generation. The different annealing processes for CuO and Cu₂O coatings play a significant role. CuO coatings are known to be more stable and less prone to degradation during annealing, which can preserve their PEC properties [34]. We have generated a table (Table 1) that presents our experimental data alongside data from previously published academic journal papers. Upon comparison, it became evident that our data outperforms the earlier research.

Table 1. Comparison of PEC measurements for CuO-coated ZnO nanorods with previous study data.

Photocurrent Enhancement	Materials and Structure	Light Source
10 mA/cm ² at 0.4 V applied bias	CuO-coated ZnO nanorods [our work]	150 W Xenon arc lamp and an AM 1.5 filter were applied to produce 100 mW/cm ² light source
0.5 mA/cm ²	CuO/ZnO core/shell heterostructure nanowire arrays [31]	100 mW white light illumination
0.4 mA/cm ²	ZnO/CuO heterojunction branched nanowires [32]	150 W xenon lamp
4.55 mA/cm ²	3D ZnO/Cu ₂ O nanowires [33]	AM1.5G illumination (100 mW/cm ²)
2.5 mA/cm ²	3D p-CuO/n-ZnO junction [54]	AM1.5G illumination (100 mWcm ⁻²)
1.0 mA/cm ²	CuO nanorod with a ZnO nanobranched protective layer [55]	1 kW xenon lamp illumination (100 mWcm ⁻²)
1.5 mA/cm ²	p-CuO/ZnO nanorod/nanobranched [34]	NA
1.0 mA/cm ²	CuO only [53]	150 W Xenon arc lamp and an AM 1.5 filter were applied to produce 100 mW/cm ² light source
2.0 mA/cm ²	CuO/ZnO nanowire heterojunction [56]	150 W Xe lamp
0.8 mA/cm ²	Copper zinc oxide heterostructure nanoflowers [57]	LED light source, no other power information
1.0 mA/cm ²	CuO/Cu ₂ O nanoflake/nanowire heterostructure [58]	150 W Xenon arc lamp and an AM 1.5 filter were applied to produce 100 mW/cm ² light source
0.4 mA/cm ² at 0.5 V applied bias	CuO-ZnO Nanostructures [35]	100 mWcm ⁻² xenon light irradiation
2.0 mA/cm ²	Cu ₂ O/CuO [4]	100 mW/cm ²

4. Conclusions

In this study, we investigated the influence of annealing conditions on copper-oxide-coated ZnO nanorods (NRs) to understand the morphological evolution and optical properties of these nanostructures. We observed distinct effects of annealing temperature and atmospheric conditions on the growth of Cu₂O and CuO on the ZnO NRs. The results indicated that annealing at specific temperatures could optimize the morphology and crystallinity of these materials. SEM images revealed the evolution of Cu₂O from silk-like to mushroom-like structures and CuO forming interconnecting nanomaterials under different annealing conditions. XRD and XPS analyses showed shifts in peak positions and binding

energies, highlighting the structural and electronic modifications induced by annealing. Moreover, photoelectrochemical measurements demonstrated that CuO-coated ZnO NRs exhibited superior photoresponse, especially under negative bias conditions, which is attributed to their favorable band structure, charge carrier separation, and stability during annealing. The findings from this research offer valuable insights into tailoring metal oxide semiconductor nanostructures for potential applications in diverse fields.

Author Contributions: Conceptualization, V.K.S.H.; methodology, Y.-C.F. and Y.-C.C.; validation, Y.-C.F., Y.-C.C. and C.-M.W.; formal analysis, V.K.S.H.; investigation, Y.-C.F.; data curation, Y.-C.F., Y.-C.C. and C.-M.W.; writing—original draft preparation, Y.-C.F. and V.K.S.H.; writing—review and editing, V.K.S.H.; supervision, V.K.S.H.; funding acquisition, V.K.S.H. All authors have read and agreed to the published version of the manuscript.

Funding: This research was funded by the Ministry of Science and Technology (MOST) of Taiwan under the project number MOST110-2221-E-260-008-MY3.

Data Availability Statement: Data are unavailable due to privacy.

Conflicts of Interest: The authors declare no conflict of interest.

References

1. Ang, T.Z.; Salem, M.; Kamarol, M.; Das, H.S.; Nazari, M.A.; Prabakaran, N. A comprehensive study of renewable energy sources: Classifications, challenges and suggestions. *Energy Strateg. Rev.* **2022**, *43*, 100939. [[CrossRef](#)]
2. Lv, J.; Xie, J.; Mohamed, A.G.A.; Zhang, X.; Wang, Y. Photoelectrochemical energy storage materials: Design principles and functional devices towards direct solar to electrochemical energy storage. *Chem. Soc. Rev.* **2022**, *51*, 1511–1528. [[CrossRef](#)] [[PubMed](#)]
3. Pitchaimuthu, S.; Sridharan, K.; Nagarajan, S.; Ananthraj, S.; Robertson, P.; Kuehnel, M.F.; Maroto-Valer, M. Solar Hydrogen Fuel Generation from Wastewater—Beyond Photoelectrochemical Water Splitting: A Perspective. *Energies* **2022**, *15*, 7399. [[CrossRef](#)]
4. Raza, A.; Zhang, X.; Ali, S.; Cao, C.; Rafi, A.A.; Li, G. Photoelectrochemical energy conversion over 2D materials. *Photochem* **2022**, *2*, 272–298. [[CrossRef](#)]
5. Chiu, Y.H.; Lai, T.H.; Kuo, M.Y.; Hsieh, P.Y.; Hsu, Y.J. Photoelectrochemical cells for solar hydrogen production: Challenges and opportunities. *APL Mater.* **2019**, *7*, 8. [[CrossRef](#)]
6. Lee, D.K.; Lee, D.; Lumley, M.A.; Choi, K.S. Progress on ternary oxide-based photoanodes for use in photoelectrochemical cells for solar water splitting. *Chem. Soc. Rev.* **2019**, *48*, 2126–2157. [[CrossRef](#)]
7. Ahnood, A.; Chambers, A.; Gelm, A.; Yong, K.T.; Kavehei, O. Semiconducting electrodes for neural interfacing: A review. *Chem. Soc. Rev.* **2023**, *52*, 1491–1518. [[CrossRef](#)]
8. Kusmirek, E. Semiconductor electrode materials applied in photoelectrocatalytic wastewater treatment—An overview. *Catalysts* **2020**, *10*, 439. [[CrossRef](#)]
9. Zheng, J.; Zhou, H.; Zou, Y.; Wang, R.; Lyu, Y.; Wang, S. Efficiency and stability of narrow-gap semiconductor-based photoelectrodes. *Energy Environ. Sci.* **2019**, *12*, 2345–2374. [[CrossRef](#)]
10. Arunachalam, M.; Kanase, R.S.; Zhu, K.; Kang, S.H. Reliable bi-functional nickel-phosphate/TiO₂ integration enables stable n-GaAs photoanode for water oxidation under alkaline condition. *Nat. Commun.* **2023**, *14*, 5429. [[CrossRef](#)]
11. Wu, H.; Zhang, D.; Lei, B.X.; Liu, Z.Q. Metal oxide based photoelectrodes in photoelectrocatalysis: Advances and challenges. *ChemPlusChem* **2022**, *87*, e202200097. [[CrossRef](#)]
12. Hassan, N.S.; Jalil, A.A.; Khusnun, N.F.; Ahmad, A.; Abdullah, T.A.T.; Kasmani, R.M.; Vo, D.V.N. Photoelectrochemical water splitting using post-transition metal oxides for hydrogen production: A review. *Environ. Chem. Lett.* **2022**, *20*, 311–333. [[CrossRef](#)]
13. Li, S.; Mo, Q.L.; Xiao, Y.; Xiao, F.X. Maneuvering cuprous oxide-based photocathodes for solar-to-fuel conversion. *Coord. Chem. Rev.* **2023**, *477*, 214948. [[CrossRef](#)]
14. Sawal, M.H.; Jalil, A.A.; Khusnun, N.F.; Hassan, N.S.; Bahari, M.B. A review of recent modification strategies of TiO₂-based photoanodes for efficient photoelectrochemical water splitting performance. *Electrochim. Acta* **2023**, *467*, 143142. [[CrossRef](#)]
15. Moridon, S.N.F.; Arifin, K.; Yunus, R.M.; Minggu, L.J.; Kassim, M.B. Photocatalytic water splitting performance of TiO₂ sensitized by metal chalcogenides: A review. *Ceram. Int.* **2022**, *48*, 5892–5907. [[CrossRef](#)]
16. Akhter, P.; Arshad, A.; Saleem, A.; Hussain, M. Recent development in non-metal-doped titanium dioxide photocatalysts for different dyes degradation and the study of their strategic factors: A review. *Catalysts* **2022**, *12*, 1331. [[CrossRef](#)]
17. Rajput, R.B.; Shaikh, R.; Sawant, J.; Kale, R.B. Recent developments in ZnO-based heterostructures as photoelectrocatalysts for wastewater treatment: A review. *Environ. Adv.* **2022**, *9*, 100264. [[CrossRef](#)]
18. Borysiewicz, M.A. ZnO as a Functional Material, a Review. *Crystals* **2019**, *9*, 505. [[CrossRef](#)]
19. Kang, Z.; Si, H.; Zhang, S.; Wu, J.; Sun, Y.; Liao, Q.; Zhang, Y. Interface engineering for modulation of charge carrier behavior in ZnO photoelectrochemical water splitting. *Adv. Funct. Mater.* **2019**, *29*, 1808032. [[CrossRef](#)]

20. Chen, W.; Qiu, Y.; Yang, S. Branched ZnO nanostructures as building blocks of photoelectrodes for efficient solar energy conversion. *Phys. Chem. Chem. Phys.* **2012**, *14*, 10872–10881. [[CrossRef](#)]
21. Liang, H.W.; Lu, Y.M.; Shen, D.Z.; Li, B.H.; Zhang, Z.Z.; Shan, C.X.; Du, G.T. Growth of vertically aligned single crystal ZnO nanotubes by plasma-molecular beam epitaxy. *Solid Stat. Commun.* **2006**, *137*, 182–186. [[CrossRef](#)]
22. Prete, P.; Lovergine, N.; Tapfer, L. Nanostructure size evolution during Au-catalysed growth by carbo-thermal evaporation of well-aligned ZnO nanowires on (100) Si. *Appl. Phys. A* **2007**, *88*, 21–26. [[CrossRef](#)]
23. Yatsui, T.; Lim, J.; Nakamata, T.; Kitamura, K.; Ohtsu, M.; Yi, G.C. Low-temperature (~270 °C) growth of vertically aligned ZnO nanorods using photoinduced metal organic vapour phase epitaxy. *Nanotechnology* **2007**, *18*, 065606. [[CrossRef](#)]
24. Singh, P.; Kumar, R.; Singh, R.K. Progress on transition metal-doped ZnO nanoparticles and its application. *Ind. Eng. Chem. Res.* **2019**, *58*, 17130–17163. [[CrossRef](#)]
25. Kumari, P.; Misra, K.P.; Chattopadhyay, S.; Samanta, S. A brief review on transition metal ion doped ZnO nanoparticles and its optoelectronic applications. *Mater. Today Proc.* **2021**, *43*, 3297–3302. [[CrossRef](#)]
26. Li, L.; ul Hasan, I.M.; He, R.; Peng, L.; Xu, N.; Niazi, N.K.; Qiao, J. Copper as a single metal atom based photo-, electro-, and photoelectrochemical catalyst decorated on carbon nitride surface for efficient CO₂ reduction: A review. *Nano Res. Energy* **2022**, *1*, e9120015.
27. Fui, C.J.; Sarjadi, M.S.; Sarkar, S.M.; Rahman, M.L. Recent advancement of ullmann condensation coupling reaction in the formation of aryl-oxygen (CO) bonding by copper-mediated catalyst. *Catalysts* **2020**, *10*, 1103. [[CrossRef](#)]
28. Dom, R.; Baby, L.R.; Kim, H.G.; Borse, P.H. Enhanced solar photoelectrochemical conversion efficiency of ZnO:Cu electrodes for water-splitting application. *Int. J. Photoenergy* **2013**, *2013*, 928321. [[CrossRef](#)]
29. Rasouli, F.; Rouhollahi, A.; Ghahramanifard, F. Gradient doping of copper in ZnO nanorod photoanode by electrodeposition for enhanced charge separation in photoelectrochemical water splitting. *Superlattices Microstruct.* **2019**, *125*, 177–189. [[CrossRef](#)]
30. Huynh, H.Q.; Pham, K.N.; Phan, B.T.; Tran, C.K.; Lee, H.; Dang, V.Q. Enhancing visible-light-driven water splitting of ZnO nanorods by dual synergistic effects of plasmonic Au nanoparticles and Cu dopants. *J. Photochem. Photobiol. A* **2020**, *399*, 112639. [[CrossRef](#)]
31. Zhao, X.; Wang, P.; Li, B. CuO/ZnO core/shell heterostructure nanowire arrays: Synthesis, optical property, and energy application. *Chem. Commun.* **2010**, *46*, 6768–6770. [[CrossRef](#)] [[PubMed](#)]
32. Kargar, A.; Jing, Y.; Kim, S.J.; Riley, C.T.; Pan, X.; Wang, D. ZnO/CuO heterojunction branched nanowires for photoelectrochemical hydrogen generation. *ACS Nano* **2013**, *7*, 11112–11120. [[CrossRef](#)] [[PubMed](#)]
33. Bai, J.; Li, Y.; Wang, R.; Huang, K.; Zeng, Q.; Li, J.; Zhou, B. A novel 3D ZnO/Cu₂O nanowire photocathode material with highly efficient photoelectrocatalytic performance. *J. Mater. Chem. A* **2015**, *3*, 22996–23002. [[CrossRef](#)]
34. Shaislamov, U.; Krishnamoorthy, K.; Kim, S.J.; Abidov, A.; Allabergenov, B.; Kim, S.; Lee, H.J. Highly stable hierarchical p-CuO/ZnO nanorod/nanobranched photoelectrode for efficient solar energy conversion. *Int. J. Hydrogen Energy* **2016**, *41*, 2253–2262. [[CrossRef](#)]
35. Albadarin, N.A.; Takriff, M.S.; Tan, S.T.; Shahahmadi, S.A.; Minggu, L.J.; Kadhum, A.A.H.; Amin, N. Tunable morphology and band gap alteration of CuO-ZnO nanostructures based photocathode for solar photoelectrochemical cells. *Mater. Res. Express* **2020**, *7*, 125010. [[CrossRef](#)]
36. Chou, C.M.; Thanh Thi, L.T.; Quynh Nhu, N.T.; Liao, S.Y.; Fu, Y.Z.; Hung, L.V.T.; Hsiao, V.K. Zinc oxide nanorod surface-enhanced Raman scattering substrates without and with gold nanoparticles fabricated through pulsed-laser-induced photolysis. *Appl. Sci.* **2020**, *10*, 5015. [[CrossRef](#)]
37. Xu, H.Y.; Chen, C.; Xu, L.; Dong, J.K. Direct growth and shape control of Cu₂O film via one-step chemical bath deposition. *Thin Solid Films* **2013**, *527*, 76–80. [[CrossRef](#)]
38. Andrievski, R.A. Review stability of nanostructured materials. *J. Mater. Sci.* **2003**, *38*, 1367–1375. [[CrossRef](#)]
39. Yang, J.; Gao, M.; Zhang, Y.; Yang, L.; Lang, J.; Wang, D.; Fan, H. Effects of annealing temperature on morphologies and optical properties of ZnO nanostructures. *Superlattices Microstruct.* **2008**, *44*, 137–142. [[CrossRef](#)]
40. Bahramian, R.; Eshghi, H.; Moshaii, A. Influence of annealing temperature on morphological, optical and UV detection properties of ZnO nanowires grown by chemical bath deposition. *Mater. Des.* **2016**, *107*, 269–276. [[CrossRef](#)]
41. Azmi, Z.H.; Mohd Aris, S.N.; Abubakar, S.; Sagadevan, S.; Siburian, R.; Paiman, S. Effect of seed layer on the growth of zinc oxide nanowires by chemical bath deposition method. *Coatings* **2022**, *12*, 474. [[CrossRef](#)]
42. Sultana, J.; Paul, S.; Karmakar, A.; Dalapati, G.K.; Chattopadhyay, S. Optimizing the thermal annealing temperature: Technological route for tuning the photo-detecting property of p-CuO thin films grown by chemical bath deposition method. *J. Mater. Sci. Mater. Electron.* **2018**, *29*, 12878–12887. [[CrossRef](#)]
43. Reyes-Vallejo, O.; Escorcía-García, J.; Sebastian, P.J. Effect of complexing agent and deposition time on structural, morphological, optical and electrical properties of cuprous oxide thin films prepared by chemical bath deposition. *Mater. Sci. Semicond. Process.* **2022**, *138*, 106242. [[CrossRef](#)]
44. Imran, M.; Asghar, G.; Tariq, G.H.; Faridi, A.W.; Bano, S.; Shifa, M.S.; Ullah, S. Investigation of annealing effects on physical properties of chemically prepared copper oxide thin films. *Results Opt.* **2023**, *10*, 100331. [[CrossRef](#)]
45. Yang, Y.; Xu, D.; Wu, Q.; Diao, P. Cu₂O/CuO bilayered composite as a high-efficiency photocathode for photoelectrochemical hydrogen evolution reaction. *Sci. Rep.* **2016**, *6*, 35158. [[CrossRef](#)]

46. Al Armouzi, N.; El Hallani, G.; Liba, A.; Zekraoui, M.; Hilal, H.S.; Kouider, N.; Mabrouki, M. Effect of annealing temperature on physical characteristics of CuO films deposited by sol-gel spin coating. *Mater. Res. Express* **2019**, *6*, 116405. [[CrossRef](#)]
47. Thirumoorthi, M.; Dhavud, S.S.; Ganesh, V.; Al Abdulaal, T.H.; Yahia, I.S.; Deivatamil, D. High responsivity n-ZnO/p-CuO heterojunction thin film synthesised by low-cost SILAR method for photodiode applications. *Opt. Mater.* **2022**, *128*, 112410. [[CrossRef](#)]
48. Seo, Y.J.; Arunachalam, M.; Ahn, K.S.; Kang, S.H. Integrating heteromixed Cu₂O/CuO photocathode interface through a hydrogen treatment for photoelectrochemical hydrogen evolution reaction. *Appl. Surf. Sci.* **2021**, *551*, 149375.
49. Akgul, F.A.; Akgul, G.; Yildirim, N.; Unalan, H.E.; Turan, R. Influence of thermal annealing on microstructural, morphological, optical properties and surface electronic structure of copper oxide thin films. *Mater. Chem. Phys.* **2014**, *147*, 987–995. [[CrossRef](#)]
50. Kim, J.; Kim, W.; Yong, K. CuO/ZnO heterostructured nanorods: Photochemical synthesis and the mechanism of H₂S gas sensing. *J. Phys. Chem. C* **2012**, *116*, 15682–15691. [[CrossRef](#)]
51. Kushwaha, A.; Moakhar, R.S.; Goh, G.K.; Dalapati, G.K. Morphologically tailored CuO photocathode using aqueous solution technique for enhanced visible light driven water splitting. *J. Photochem. Photobiol. A* **2017**, *337*, 54–61. [[CrossRef](#)]
52. Wojcieszak, D.; Obstarczyk, A.; Mańkowska, E.; Mazur, M.; Kaczmarek, D.; Zakrzewska, K.; Domaradzki, J. Thermal oxidation impact on the optoelectronic and hydrogen sensing properties of p-type copper oxide thin films. *Mater. Res. Bull.* **2022**, *147*, 111646. [[CrossRef](#)]
53. Altaf, C.T.; Coskun, O.; Kumtepe, A.; Rostas, A.M.; Iatsunskyi, I.; Coy, E.; Sankir, N.D. Photo-supercapacitors based on nanoscaled ZnO. *Sci. Rep.* **2022**, *12*, 11487. [[CrossRef](#)] [[PubMed](#)]
54. Wu, F.; Cao, F.; Liu, Q.; Lu, H.; Li, L. Enhancing photoelectrochemical activity with three-dimensional p-CuO/n-ZnO junction photocathodes. *Sci. China Mater.* **2016**, *59*, 825–832. [[CrossRef](#)]
55. Shaislamov, U.; Krishnamoorthy, K.; Kim, S.J.; Chun, W.; Lee, H.J. Facile fabrication and photoelectrochemical properties of a CuO nanorod photocathode with a ZnO nanobranch protective layer. *RSC Adv.* **2016**, *6*, 103049–103056. [[CrossRef](#)]
56. Tsege, E.L.; Cho, S.K.; Tufa, L.T.; Tran, V.T.; Lee, J.; Kim, H.K.; Hwang, Y.H. Scalable and inexpensive strategy to fabricate CuO/ZnO nanowire heterojunction for efficient photoinduced water splitting. *J. Mater. Sci.* **2018**, *53*, 2725–2734. [[CrossRef](#)]
57. Wojtyła, S.; Baran, T. Copper zinc oxide heterostructure nanoflowers for hydrogen evolution. *Int. J. Hydrog. Energy* **2019**, *44*, 27343–27353. [[CrossRef](#)]
58. John, S.; Roy, S.C. CuO/Cu₂O nanoflake/nanowire heterostructure photocathode with enhanced surface area for photoelectrochemical solar energy conversion. *Appl. Surf. Sci.* **2020**, *509*, 144703. [[CrossRef](#)]

Disclaimer/Publisher's Note: The statements, opinions and data contained in all publications are solely those of the individual author(s) and contributor(s) and not of MDPI and/or the editor(s). MDPI and/or the editor(s) disclaim responsibility for any injury to people or property resulting from any ideas, methods, instructions or products referred to in the content.